

¹ **A Wall-like Sharp Downward Branch of the Walker**
² **Circulation above the Western Indian Ocean**

Tsubasa Kohyama¹, Tamaki Suematsu², Hiroaki Miura³, and Daisuke

Takasuka⁴

3 Key points:

4 • Climatology and interannual variability of the sharp downward branch above the Indian
5 Ocean are discussed.

6 • Model experiments confirm that the sharp downward branch is sustained by East African
7 topography, in addition to radiative cooling.

8 • Without mountains in East Africa, the eastern Horn of Africa would exhibit wetter and
9 more convective climatology.

Corresponding author: T. Kohyama, Department of Information Sciences, Ochanomizu Uni-
versity, 2-1-1, Otsuka, Bunkyo-ku, Tokyo, 112-8610, Japan. (tsubasa@is.ocha.ac.jp)

¹Department of Information Sciences,
Ochanomizu University, Tokyo, Japan.

²Atmosphere and Ocean Research
Institute, The University of Tokyo, Tokyo,
Japan.

³Department of Earth and Planetary
Science, The University of Tokyo, Tokyo,
Japan.

⁴Japan Agency for Marine-Earth Science
and Technology, Yokohama, Japan.

10 **Abstract.** In the zonal direction, the downward branch of the Walker cir-
11 culation above the Indian Ocean is only 20 degrees wide, whereas the Pa-
12 cific counterpart is 90 degrees wide. This zonal sharpness is notable because
13 atmospheric disturbances smaller than the planetary scale, such as the Asian
14 Summer Monsoon, can interact with the planetary-scale Walker circulation
15 through this branch. As a moist circulation, this zonal sharpness is imprinted
16 on a unique zonal discontinuity of the tropical rain belt above Northeast Africa.
17 Therefore, in this study, we refer to this narrow downward branch as the “Wall”,
18 investigate its climatology and interannual variability, and aim at determin-
19 ing its reason for existence.

20 The strongest season of the lower tropospheric Wall in boreal summer is
21 sustained by horizontal cold advection associated with the Asian Summer
22 Monsoon. Two weak phases of the Wall correspond to two rainy seasons at
23 the Eastern Horn of Africa, which are not reproduced well by state-of-the-
24 art global climate models. As for interannual variability, one standard de-
25 viation change of a strength of the downward motion at the Wall is associ-
26 ated with about one degree of sea surface temperature variation in the trop-
27 ical Pacific, and the regression and correlation coefficients are highest in bo-
28 real autumn. Nevertheless, total variance is explained more by local sea sur-
29 face temperature.

30 Experiments using a convection-permitting atmospheric model show that
31 vertical mixing forced by mountain waves in East Africa are necessary for

³² sustaining the Wall. After flattening the East African topography, zonal dis-
³³ continuity of the tropical rain belt disappears.

1. Introduction

34 The Walker circulation is the most prominent planetary-scale tropical atmospheric cir-
35 culation in the zonal direction [e.g., *Walker*, 1923, 1924; *Bjerknes*, 1969]. It has been
36 understood that, to first order, the vertical motion associated with the Walker circulation
37 consists of upward branches over relatively warm surfaces (e.g., the warm pool in the
38 western Pacific) and downward branches over relatively cool surface (e.g., the cold tongue
39 in the eastern Pacific) [e.g., *Lau and Yang*, 2003]. In the context of climate variability,
40 trends and interannual variability of the Walker circulation have long been investigated
41 in association with climate modes and the greenhouse gas forcing [e.g., *Tanaka et al.*,
42 2004]. In particular, the Pacific branches of the Walker circulation have received much
43 attention, because its interannual fluctuation serves as the atmospheric component of the
44 El Niño Southern Oscillation (ENSO), the most dominant interannual climate mode on
45 Earth [e.g., *Bjerknes*, 1969].

46 As a mean state, however, a downward branch of the Walker circulation above the
47 western Indian Ocean also exhibits a strong subsidence, which is at least comparable to
48 the Pacific downward branch. Figure 1a shows the annual-mean equatorial vertical motion
49 calculated by taking the meridional mean over the equatorial region (10°S-10°N). The
50 strong and sharp downward branch stands at the western edge of the Indian Ocean (40°E-
51 60°E), whereas the weak and wide downward branch lies over the eastern Pacific (90°W-
52 150°W). Considering the size of the two oceanic basins, one might find this interbasin
53 contrast counterintuitive.

54 In fact, the interbasin difference in apparent strength of the downward motion em-
55 anates from latitudinal dependence. An important caveat of this meridional-mean view
56 shown in Fig. 1a is that the strength of the downward motion depends upon latitudinal
57 choices of the equatorial belt, as confirmed by *Schwendike et al.* [2014] who defined the
58 *local* Walker circulation by shifting the equatorial belt southward (35°S - 10°N) when tak-
59 ing this meridional mean. Figure 2a shows the annual-mean meridional-mean equatorial
60 vertical motion over the equatorial belt of 10°S - 10°N , 5°S - 5°N , and 2°S - 2°N . While the
61 downward branch above the Indian Ocean relatively keeps its strength notwithstanding
62 the latitudinal choices, that of the eastern Pacific becomes stronger when narrower equa-
63 torial belts are chosen. A key to understand this difference is the zonal-mean crosssection
64 (Fig. 2b). The outstanding difference between the Indian and the Pacific downward
65 branches is the degree of meridional asymmetry. The apparent weak downward motion
66 above the Pacific, shown in Fig. 1a, originates from an offset of a strong upward branch
67 over the northern off-equatorial region (4°N - 10°N) against a strong equatorial downward
68 motion over 10°S - 2°N . On the other hand, the downward branch above the Indian Ocean
69 shown in Fig. 1a consists of a strong downward branch over 4°S - 10°N with a hint of weak
70 upward branch located to the south. Though it could be misleading in some context, we
71 will carefully keep using the equatorial belt of 10°S - 10°N in this study, because we are
72 interested in the meridionally-broad equatorial downward branch above the Indian Ocean.

73 A more fundamental difference between the two downward branches lies in the longi-
74 tudinal width. That is, the downward branch above the Indian Ocean is only 20 degrees
75 thick in the zonal direction, whereas the Pacific counterpart is about 90 degrees wide. As
76 we shall see in later sections, this zonal sharpness of the Indian Ocean branch is remark-

77 able in the sense that phenomena smaller than the planetary scale, such as the Asian
78 Summer Monsoon and possibly mountain waves, can easily interact with the planetary-
79 scale Walker circulation via this branch. This zonal sharpness is particularly notable in
80 the lower tropospheric layer, where the downward branch subsides only onto the coastal
81 western Indian Ocean and not onto the African continent (Fig. 2c), which is consistent
82 with *Yang et al.* [2015]. In addition, from the viewpoint of moist circulations, the narrow
83 downward branch is imprinted on a unique zonal discontinuity of the tropical rain belt.
84 Figures 1b, 1c, and 1d show the annual-mean vertical motion at 500 hPa, outgoing long-
85 wave radiation (OLR), and precipitation, respectively, over the tropics. The tropical rain
86 belt is typically characterized by the narrow convective band that circles the Earth along
87 the equatorial region [e.g., *Nicholson*, 2018], but if we carefully look at the tropical rain
88 belt, a discontinuity is found at the western edge of the Indian Ocean.

89 One of the major implications of this tropical rain belt discontinuity, and thereby, of
90 the narrow downward branch, is the relatively dry climate at the so-called “Eastern Horn
91 of Africa”, whose mean state, annual cycle, variability, and change have long been inves-
92 tigated in many previous studies [e.g., *Camberlin*, 1995; *Schreck III and Semazzi*, 2004;
93 *Liebmann et al.*, 2014; *Lyon*, 2014; *Tierney et al.*, 2015; *Liebmann et al.*, 2017]. In this
94 regard, *Zhao and Cook* [2021] recently examined the influence of the narrow downward
95 branch on East African rainfall. Another recent work by *King et al.* [2021] also demon-
96 strated, based on the model ensemble that participated in the Coupled Model Intercom-
97 parison Project Phase 5 (CMIP5), that the poor representation of the narrow downward
98 branch explains rainfall biases over Kenya during the main East African rainy seasons.
99 In addition, the sensitivity of the climate in this region to topography in East Africa has

100 long been examined from multiple perspectives [e.g., *Slingo et al.*, 2005; *Naiman et al.*,
101 2017; *Munday et al.*, 2021]. In line with these previous studies, by exploring the physics of
102 the narrow downward branch in a comprehensive way, we expect a better understanding
103 of the climatology of the Eastern Horn of Africa, whose annual cycle of precipitation is
104 poorly reproduced by state-of-the-art, air-sea coupled global climate models [*Yang et al.*,
105 2014; *Tierney et al.*, 2015].

106 Therefore, in this study, we refer to this meridionally-wide, zonally-narrow sharp down-
107 ward branch above the Indian Ocean as the “Wall” of the Walker Circulation, and will
108 investigate its climatology and interannual variability in the hope that its reason for exis-
109 tence will be determined. Data and methods are described in the next section. In section
110 3, we describe the seasonality of the Wall, and highlight a role of horizontal cold advection
111 to support its strongest phase. Next, in section 4, we define the Wall index to describe
112 the interannual variability of the Wall and point out that both remote and local SST
113 explain the interannual variance. In section 5, we then perform model experiments to
114 identify the East African topography as a necessary condition for the existence of the
115 Wall, and discuss implications for the climate at the Eastern Horn of Africa. Conclusions
116 are presented in section 6.

2. Data and Model

2.1. Data

117 Observed vertical motion, wind, and temperature data are from the European Center for
118 Medium range Weather Forecasting (ECMWF) ERA-Interim reanalysis data [*Dee et al.*,
119 2011]. Observed OLR data is from the National Oceanic and Atmospheric Administration
120 (NOAA) interpolated OLR [*Liebmann and Smith*, 1996]. Observed precipitation data is

121 from the Global Precipitation Climatology Project (GPCP) [Adler *et al.*, 2003]. The time
122 span of the atmospheric data used in this study is from 1979 through 2017. The horizontal
123 resolutions used in this study are 3° for vertical motion, wind, and temperature, and
124 2.5° for OLR and precipitation. Observed SST data is from the National Oceanic and
125 Atmospheric Administration (NOAA) Optimum Interpolation SST (OISST) [Reynolds
126 *et al.*, 2007]. Only when the relationship between atmospheric variables and SST is
127 analyzed, the data from 1982 through 2017 is used, due to the availability of the satellite-
128 based SST dataset. The resolution of the SST data is 1° in both longitudes and latitudes.

2.2. Atmospheric General Circulation Model (AGCM) experiments

129 We use the Nonhydrostatic Icosahedral Atmospheric Model (NICAM) [Tomita *and*
130 *Satoh*, 2004; *Satoh et al.*, 2008, 2014], the version of which used for our experiments is the
131 latest stable version, NICAM16-S [Kodama *et al.*, 2020]. The condensation processes are
132 explicitly calculated using the single moment water 6 microphysics scheme [Tomita, 2008].
133 Sub-grid scale turbulence is calculated by a modified version of the Mellor-Yamada scheme
134 [Mellor *and Yamada*, 1982; *Nakanishi and Niino*, 2004; *Noda et al.*, 2010]. The radia-
135 tion model with two stream radiative transfer scheme employs a correlated k -distribution
136 method (mstrnX) [Sekiguchi *and Nakajima*, 2008]. Surface fluxes are calculated with a
137 modified version of the Louis scheme [Louis, 1979; *Uno et al.*, 1995]. For the land pro-
138 cesses, the minimal advanced treatments of surface interaction and runoff (MATSIRO)
139 land model [Takata *et al.*, 2003] is used. Orographic gravity wave drag is considered to
140 be sufficiently resolved in our simulations to obviate the need for parameterization of this
141 process at subgrid scale.

142 The horizontal resolution is approximately 14 km on an icosahedral hexagonal-
143 pentagonal mesh [Tomita *et al.*, 2002]. A terrain-following vertical grid coordinate is
144 employed with the model top of approximately 40 km and 38 vertical layers, whose thick-
145 ness increases with height. The model time step is 60 seconds. Our simulations are ini-
146 tialized on 00 UTC 28 June 2013 and 2016, and are integrated for 93 days for each year.
147 Initial conditions of the atmosphere and the ocean are derived from the National Cen-
148 ters for Environmental Prediction (NCEP) Final Operational Model Global Tropospheric
149 Analysis (NCEP-FNL) [NCEP, 2015]. Time evolution of the sea surface temperature
150 is prescribed externally from the interpolation of the NCEP-FNL data at 00 UTC on
151 each day. To mitigate the effect of the model bias over land, the initial conditions of the
152 land surface are taken from the monthly climatology derived from the last 5 years of a
153 10-year simulation of NICAM at 220 km horizontal resolution following Kodama *et al.*
154 [2015, 2020].

155 Because it takes approximately 45 days for the values of vertical motions to converge to
156 realistic climatological values, the first 63 days of the integrations are taken as a spin-up
157 period, and the last 30 days of the integrations starting from 1 September are analyzed
158 in this study. For comparison, we have also performed the same simulation but initialized
159 on 00 UTC 28 April 2016 to capture the strongest month of the Wall, i.e., July. Clima-
160 tology of the Walker circulation, however, is not reproduced well, presumably because the
161 observed downward branches are not established until the end of May, during which the
162 integration cannot be used as a spin-up period to capture the target circulation. Related
163 difficulty in this season is also discussed by King *et al.* [2021] in association with dry biases
164 (i.e., too strong subsidence) in AMIP experiments by the CMIP5 models. Though the

165 AGCM used in this study realistically simulates the mean field over long time periods, the
166 reproducibility of quick variations within relatively short time scales, such as a transition
167 of seasons, is insufficient, to which future improvement is needed.

168 In addition to control runs, we have performed an experiment named “Flat East Africa
169 (FEA)”, in which the elevations are set to be 1 meter over the entire East African region
170 (30°S - 30°N , 30°E - 50°E) (see Fig. 9a) for 2013 (ENSO neutral) and 2016 (La Niña). We
171 have also performed the same experimental sets but for 2015, an El Niño year, but the
172 control run does not reproduce the observed features of the Walker circulation. This poor
173 reproducibility of the Wall during an El Niño year appears to be because the observed
174 Wall is weaker than those of other years (see Fig. 6b). In our model, the water vapor
175 supply from the anomalously warm eastern equatorial Pacific is biased to be excessive.
176 The Walker Circulation over the tropics is distorted by this bias, to which the zonally-thin
177 downward branch is sensitive. Therefore, in this study, only AGCM experiments in ENSO
178 neutral and La Niña years will be discussed.

3. Climatology of the Wall

179 In this section, we first overview the seasonality of the Wall and the consistency with
180 the local rainy seasons. Then, from the energetic viewpoint, we show that the strongest
181 phase of the Wall is supported by horizontal cold advection associated with the Asian
182 Summer Monsoon.

3.1. Bimodal seasonality of the Wall

183 The Wall exhibits bimodal seasonal variability in its strength of the subsidence. The
184 left panels of Fig. 3 shows the monthly climatological-mean equatorial vertical motion

185 averaged over the base period of 1979-2017. The Wall exhibits moderate subsidence from
 186 January through March, almost disappears from April through May, reaches its strongest
 187 phase from June through September, and becomes weak from October through December.

188 The phase of this bimodal seasonality corresponds well to the annual precipitation
 189 cycle of the Eastern Horn of Africa, where two rainy seasons are known to exist. In this
 190 region, the term “Long Rains” denotes the longest and wettest rainy season that lasts
 191 from March through May, and the term “Short Rains” denotes the shorter and drier rainy
 192 season that peaks in October. As *King et al.* [2021] recently showed based on analyses
 193 of the CMIP5 model ensemble, the insufficient representation of this bimodality by state-
 194 of-the-art global climate models [*Tierney et al.*, 2015] (i.e., the models produce excessive
 195 “Short Rains” and insufficient “Long Rains”) is inseparable from the reproducibility of
 196 the seasonal variability of the Wall.

3.2. MSE framework to understand the energy balance for sustaining the Wall

197 Hereafter, under the moist static energy (MSE) framework (e.g. Neelin and Held 1987),
 198 the heat budget of the Wall will be discussed. The definition of MSE is as follows:

$$\text{MSE} = C_p T + Lq + gz \quad (1)$$

199 where C_p is the specific heat capacity, T is air temperature, L is the latent heat of con-
 200 densation, q is specific humidity, g is the gravitational acceleration, and Z is geopotential
 201 height.

202 When this framework is applied to the budget at a constant height in the Wall region,
 203 the Lq term is of second order importance assuming that the Wall region is dry enough:

$$\left. \frac{\partial(\text{MSE})}{\partial t} \right|_{z=\text{const.}} = C_p \left. \frac{\partial T}{\partial t} \right|_{z=\text{const.}} + L \left. \frac{\partial q}{\partial t} \right|_{z=\text{const.}} \simeq C_p \left. \frac{\partial T}{\partial t} \right|_{z=\text{const.}} \quad (2)$$

204 Hence, the temperature tendency is of greatest interest, which is also employed by *Veiga*
 205 *et al.* [2011].

206 To understand climatological vertical air motion, the MSE tendency, and thereby tem-
 207 perature tendency, is assumed to be negligible so that the following steady-state balance
 208 is sustained:

$$\frac{\partial \bar{T}}{\partial t} \Big|_{z=\text{const.}} = -\bar{v} \cdot \nabla_h \bar{T} - \bar{w} \left(\frac{\partial \bar{T}}{\partial z} + \Gamma_d \right) + (\text{eddy transport}) + (\text{diabatic heating}) \simeq 0 \quad (3)$$

209 where the overlines denote temporal mean values, the $-\bar{v} \cdot \nabla_h \bar{T}$ term denotes horizontal
 210 temperature advection, w denotes vertical motion, and Γ_d denotes the dry adiabatic lapse
 211 rate. This balance yields the following formula:

$$(\text{subsidence}) \propto (\text{horizontal cold advection}) + (\text{eddy cooling}) + (\text{diabatic cooling}) \quad (4)$$

212 In this study, one of our goals is to determine which terms in Eqn. 4 are of first-order
 213 importance at each vertical level through the tropospheric Wall. In general, within the
 214 tropics, adiabatic heating of large-scale downward motion is balanced with diabatic cooling
 215 (i.e., radiative cooling), and this energy budget is mostly true for the Walker circulation
 216 as well [*Veiga et al.*, 2011]. In the Wall region, however, we will show that horizontal cold
 217 advection and eddy cooling are of first-order importance to sustain the lower and upper
 218 tropospheric downward motion, respectively.

3.3. Role of horizontal cold advection in the strongest phase of the Wall

219 One of the essential features of the strongest phase of the Wall is that the subsidence
 220 reaches the surface, which is not the case in weaker phases (Fig. 3). To sustain the Wall,
 221 horizontal temperature advection plays a key role for lower tropospheric atmospheric
 222 subsidence to extend to the surface. The right panels of Fig. 3 shows the mean horizontal

223 temperature advection, which is defined as the inner product of climatological horizontal
224 wind and the horizontal gradient of climatological temperature. Our definition of the
225 mean horizontal advection does not take eddy heat transport into account.

226 The strongest subsidence observed in the lower troposphere from June through Septem-
227 ber is supported by the mean horizontal advection, and the horizontal cold advection is
228 tightly connected to the Asian Summer Monsoon. Figure 4 show vertical-mean views of
229 the horizontal temperature advection decomposed into zonal and meridional components.
230 The horizontal advection cools the Wall region in boreal summer, when the Wall reaches
231 its maximum phase (Fig. 4, top). This horizontal advection is realized by the meridional
232 advection (Fig. 4, bottom right), rather than the zonal component (Fig. 4, bottom left).
233 In Fig. 5, these components are further decomposed into zonal wind, zonal temperature
234 gradient, meridional wind, and meridional temperature gradient. Based on these panels,
235 the maximum horizontal advection in boreal summer originates from the southerly winds
236 associated with Asian Summer Monsoon, which blow toward the upgradient direction of
237 the temperature field in this season.

238 Presumably, the aforementioned cooling effect drags down the lower tropospheric Walker
239 Circulation to the surface, which is capable of strengthening the downward flow of the Wall
240 further. This notion is consistent with the disappearance of the Wall from April through
241 May, because this season is the period when the Asian summer monsoon is weakened to
242 switch its direction before the onset of the strong Somali jet in early June [e.g., *Findlater*,
243 1969]. From an energetic viewpoint, the relevance of the Somali jet is also consistent with
244 *Heaviside and Czaja* [2013], who showed that the Somali jet dominantly accomplishes the
245 atmospheric cross-equatorial heat transport.

4. Interannual variability of the Wall

246 In this section, we define the Wall index to point out that both remote and local sea
247 surface temperature (SST) variability explains the interannual variations of the Wall.

4.1. Definition of the Wall index

248 To highlight the interannual variability of the Wall, we define the Wall index as the
249 average over vertical motions at 250, 550, and 850 hPa. This index should be physically
250 interpreted as the mass-weighted average of vertical motions for the upper (100-400 hPa),
251 middle (400-700 hPa), and lower (700-1000 hPa) tropospheric layers. Figure 6a shows that,
252 to first order, the downward motion for the interannual scale is vertically constant, which
253 justifies the definition of the Wall index for the purpose of representing the downward
254 motion throughout the troposphere.

4.2. Relationship with ENSO, IOD, and local SST variability

255 The interannual variability of the Wall is explained by ENSO, which reminds us of the
256 notion that the Wall is a part of the Walker circulation. The top panel of Fig. 6b shows
257 the 5-month running-meaned timeseries of the Wall index. Also shown is the 5-month
258 running-meaned Niño 3.4 index, which is defined as SST anomalies averaged over the Niño
259 3.4 region (5°S - 5°N , 170°W - 120°W), but the sign is reversed. These two indices exhibits
260 a correlation of 0.54 (1982-2017), which is significant at the 95% confidence level. During
261 an El Niño event, the Wall region exhibits a weakly downward motion, and vice versa for
262 a La Niña event. In particular, the strong negative peaks of the Wall index in 1982, 1997,
263 and 2015 are well-explained by big El Niño events, whereas the strong positive peaks of
264 the Wall index in 1998, 2010, and 2016 are well-explained by big La Niña events.

265 In addition to ENSO, the Indian Ocean Dipole (IOD) [*Saji et al.*, 1999] also explains
266 the Wall index well. The bottom panel of Fig. 6b is the same as top but for the 5-month
267 running-meaned Dipole Mode index, which is defined as the SSTA difference calculated
268 in the manner of the western equatorial Indian Ocean (50°E-70°E and 10°S-10°N) minus
269 the south eastern equatorial Indian Ocean (90°E-110°E and 10°S-0°N). The correlation
270 between the Wall index and the Dipole Mode index is 0.63 (1982-2017), which is significant
271 at the 95% confidence level. During a negative IOD event, the Wall region exhibits a
272 similar response to a La Niña event, though some of which could be explained by the
273 covariance between ENSO and IOD.

274 The association with ENSO and IOD is also verified by SST spatial patterns. Figure
275 6c shows the regression map of SST anomalies on the monthly-mean Wall index. This
276 map clearly shows that the Wall variability is projected onto the equatorial Pacific SST
277 variability. Because interannual variance of the tropical SST variability in the Pacific
278 is dominated by ENSO, it is virtually certain that ENSO is one of the key factors to
279 understand the Wall climate variability. That being said, the clear regression pattern in
280 the Pacific does not necessarily mean that the Wall variance is predominantly explained
281 by ENSO. Figure 6d shows the same map as Fig. 6c but for correlation coefficients. Based
282 on this correlation map, though ENSO still retains its importance, local SST variability,
283 particularly an IOD-like zonal SST gradient, explains more variance of the Wall. Also
284 notable is the high positive correlations over the maritime continent, presumably because
285 the strength of the upward motions allowed in this region is also inseparable from the
286 amount of the downward motions realized in the whole tropics, following the continuity
287 equation.

288 The association with SST patterns are seasonally dependent. Figure 7 shows that cor-
289 relations between the Wall index and the other climate indices reach their maxima during
290 boreal autumn, which corresponds to the season of the “Short Rains”, while the connec-
291 tion to the “Long Rains” season is weaker. This seasonal dependence is also confirmed by
292 the SST regression and correlation patterns shown in Fig. 8. Our result is consistent with
293 previous studies [e.g., *Ogallo*, 1988; *Camberlin and Philippon*, 2002] that showed that,
294 while the “Short Rains” are closely related to ENSO, the “Long Rains” do not exhibit
295 as strong linkage to external climate forcings, possibly because the ENSO is more active
296 in boreal autumn [e.g., *Hastenrath et al.*, 2002]. That being said, our result also exhibits
297 weak but significant correlations in MAM, which is consistent with other previous studies
298 [*Williams and Funk*, 2011; *King et al.*, 2021].

5. Role of the East African topography for sustaining the Wall

299 Though we have concluded in section 3 that strong subsidence in the lower troposphere
300 is associated with horizontal temperature advection, it remains unexplored what makes
301 the subsidence in the Wall so strong that the Wall penetrates the entire troposphere in the
302 vertical direction. In particular, cooling mechanisms of the upper troposphere have been
303 largely unexplored. Therefore, in this section, we perform model experiments to highlight
304 the role of topography for sustaining the Wall. Some implications for the climate of the
305 Eastern Horn of Africa are also discussed.

5.1. Background

306 Our experiments are inspired by *Naiman et al.* [2017], who showed, in an interesting way,
307 that topography can play major roles in determining the tropical circulation. Using the

308 Geophysical Fluid Dynamics Laboratory (GFDL)-Earth System Model (ESM) 2M, they
309 performed an experiment called “Pancake”, in which they removed all the topography
310 on Earth and simulated the air-sea coupled system with flat lands. Because the Wall
311 disappears in their “Pancake” run, we have hypothesized that, by flattening topography
312 regionally rather than globally, it is possible to pinpoint the location of mountains that
313 directly contribute to the realization of the Wall.

314 In this regard, at the end of last century, *Rodwell and Hoskins* [1995] already pointed
315 out the importance of East African Highlands for the existence of the Somali jet by
316 flattening the topography in this region as well as disabling the land-sea contrast in
317 surface friction in their model. Furthermore, *Ogwang et al.* [2014] also investigated a
318 precipitation response to regionally flattened African topography and demonstrated that
319 the mean rainfall significantly reduces to the west of the Wall region. Considering their
320 results, by eliminating the topography in East Africa, the strength and the hydrology at
321 the center of the Wall may also be modulated.

5.2. Model experiments with flat East African topography

322 In this study, in addition to a control run, the FEA experiment is arranged where the
323 East African topography is flattened in the region shown in Fig. 9a (see also the Data
324 and Model section). The top and middle panels of Fig. 9b shows the monthly-mean
325 equatorial vertical motion in September 2013 (ENSO neutral) and 2016 (La Niña) based
326 on observations and the control experiment, respectively. The control runs in both years
327 simulates the observed vertical motion associated with the Walker circulation well, so it
328 is justified to investigate the Wall using this AGCM.

329 The FEA experiment reveals that, without the East African topography, the Wall dis-
 330 appears almost entirely through the troposphere (Fig. 9b, bottom). By comparing the
 331 control and FEA runs, at least in both 2013 and 2016, the East African topography is a
 332 necessary condition for existence of the Wall.

333 A promising hypothesis is that the lack of turbulence generated by mountain waves
 334 suppresses vertical mixings. Because the lower troposphere generally has lower potential
 335 temperature than the upper troposphere, the reduction of vertical heat exchange weakens
 336 the subsidence of upper tropospheric air. Figure 10a shows the difference of equatorial
 337 vertical motions between the control and FEA runs, which should be interpreted as the
 338 downward motion forced by the East African topography. In this model, the downward
 339 branch is shifted westward compared to observations, so 30°E-45°E is drawn. Also shown
 340 in the left panel of Fig. 10b is the energetic tendency contributions by the sum of eddy
 341 heat transport (EHT) and longwave radiation. Here, the EHT contribution is calculated
 342 as follows.

$$\text{EHT} = -\frac{\overline{\partial u' T'}}{\partial x} - \frac{\overline{\partial v' T'}}{\partial y} - \frac{\overline{\partial w' T'}}{\partial z} \quad (5)$$

343 where x , y , and z denotes zonal, meridional, and vertical coordinates, respectively; u , v ,
 344 and w denotes zonal wind, meridional wind, and vertical motion, respectively; T denotes
 345 temperature. The overlines denote the mean over September simulated in the model, and
 346 the primes denote deviations from the mean.

347 EHT and longwave radiation explain how East African topography works for realizing
 348 the vertical motion. In particular, the downward motion at higher levels than 10 km
 349 is predominantly explained by the eddy heat transport (Fig. 10b, middle). The phase
 350 of heat and momentum transport is shifted, which suggests a hint of stationary gravity

351 waves forced by mountains. Because the mountain waves suppress the upper tropospheric
352 cloudiness, radiative cooling is enhanced in the middle tropospheric layer (Fig. 10b, right),
353 which in turn strengthens the downward motion further.

354 A caveat of this heat budget analysis is that the cooling effects of eddy transport and
355 longwave radiation are quantitatively insufficient to explain the total downward motion.
356 By assuming the dry adiabatic lapse rate, the vertical motion of 500 m/day requires ap-
357 proximately 5 °C/day of cooling, but the aforementioned effects only explains 1 °C/day
358 of cooling. Though a more dominant effect may exist, it is still hard to close perfectly
359 the heat budget based on an analysis of the 6-hourly snapshots available in our AGCM.
360 Nevertheless, by using the convection permitting model without artificial gravity wave
361 drags, our experiments at least confirm that the upper tropospheric downward motion
362 is sustained by eddy heat transport forced by East African topography, rather than ra-
363 diative cooling. Radiative cooling, enhanced by the clearer condition, is only capable of
364 contributing the downward motion in lower altitudes where specific humidity is higher.

365 This vertical mixing effect serves as a good example where interscale interaction plays
366 a fundamental role in downward branches, in addition to convective upward branches, to
367 realize the large-scale atmospheric circulation in the current tropical climate. Specifically,
368 the narrowly localized downward branch above the western Indian Ocean is realized as a
369 result of interactions between large-scale motions and disturbances in smaller horizontal
370 scales than the weak temperature gradient approximation [*Sobel et al.*, 2001].

5.3. Implications for the climate of the Eastern Horn of Africa

371 Without the East African topography, the relatively dry climate at the Eastern Horn
372 of Africa would become wetter than in the real world. Figure 11 shows the monthly-

373 mean OLR and precipitation near the Wall in 2013 and 2016. The control run of the
374 high-resolution convection-permitting model reproduces both OLR and precipitation well,
375 particularly the discontinuity of the tropical rain belt. In the FEA run, as the East African
376 topography is flattened, the discontinuity of the tropical rain belt disappears, which results
377 in extension of the tropical rain belt over East Africa. Our result is consistent with a
378 model experiment without topography performed by *Chou and Neelin* [2003], which does
379 not exhibit the discontinuity of the tropical rain belt.

380 Both local processes and remote forcings can contribute to the “closing” of the trop-
381 ical rain belt discontinuity in the FEA run. Locally, the removal of the Wall enhances
382 convection above the Eastern Horn of Africa. This enhancement is due to the reduction
383 of large-scale atmospheric subsidence as discussed in the last subsection. In addition to
384 this local instability effect, clouds and moist air, which are advected remotely by zonal
385 winds, are also allowed to enter the Eastern Horn of Africa from the interior of the African
386 continent, because topographic obstacles do not exist.

6. Summary and Discussions

387 We have reconsidered the climatology and the interannual variability of the Walker
388 circulation by focusing on its sharp downward branch, which we refer to as the Wall,
389 observed at the western edge of the Indian Ocean (Figs. 1 and 2). A distinctive feature
390 of the Wall is the two-peak seasonality (Fig. 3). The two weak phases of the Wall,
391 one in boreal spring and the other in boreal autumn, correspond well to the two rainy
392 seasons at the Eastern Horn of Africa, which is not reproduced well by state-of-the-art
393 GCMs. Another distinctive feature is that the subsidence of the Wall in its strongest
394 phase reaches the surface (Figs. 1 and 3). This “subsidence extension” appears to be

395 sustained by horizontal cold advection associated with the Asian Summer Monsoon (Figs.
396 3-5).

397 The interannual variability of the Wall is in no doubt associated with ENSO, but more
398 variance is explained by SSTs in western equatorial Indian Ocean and over the maritime
399 continent (Fig. 6). This kind of association between the Wall and the tropical SST is
400 strongest in boreal autumn (Figs. 7 and 8), as suggested by *Hastenrath et al.* [2002] and
401 many others. Nevertheless, our result also exhibits weak but significant correlations in
402 boreal spring, which is consistent with some previous studies that focused on the Indian
403 Ocean component of the Walker circulation in this season [*King et al.*, 2021; *Williams and*
404 *Funk*, 2011]. Because these observational pieces of evidence in our present work are based
405 on a single reanalysis dataset, further verifications using multiple datasets are needed. In
406 particular, a more up-to-date version of the ECMWF analysis, ERA5, could be of interest
407 as a potential candidate for this purpose.

408 AGCM experiments show that the East African topography determines the strength of
409 the Wall (Fig. 9). In the FEA experiment, where the East African mountains are broadly
410 flattened, the Wall almost vanishes throughout the entire tropospheric layer. This result
411 leads to a conclusion that the East African topography is necessary for the existence of
412 the Wall. We hypothesize that the role of topography is to generate mountain waves
413 in response to large-scale circulation. The stationary vertical mixing enhances vertical
414 heat exchange to cool the upper troposphere, which makes the Wall rigid (Fig. 10).
415 Assuming this mechanism, climate variability of the Wall could also be understood based
416 on interscale interactions between global-scale circulation and local-scale mountain waves.
417 In addition, we could also hypothesize that the modulation of the Somali jet [*Chakraborty*

418 *et al.*, 2009] and the Turkana low-level jet [*Nicholson*, 2016; *Hartman*, 2018; *Vizy and*
419 *Cook*, 2019] by the African topography could control the lower tropospheric downward
420 motion. Our simulation, however, does not reproduce the lower tropospheric downward
421 motion realistically enough to make a case for the role of horizontal advection. Further
422 process studies are needed to improve the robustness of these physical processes.

423 An implication of our conclusion is that the dry and clear climate at the Eastern Horn
424 of Africa is sustained by the East African topography (Fig. 9). As a local effect, the large-
425 scale subsidence associated with the Wall suppresses the local convection by drying the
426 environment and by suppressing upward motion. At the same time, the high mountains in
427 East Africa serve as obstacles that prevent clouds and moist air from being conveyed from
428 the interior of the African continent. Because both of these local and remote processes are
429 inseparable from the existence of the East African topography, it remains to be an open
430 question which process serves as the dominant cause of the tropical rain belt discontinuity.

431 **Acknowledgments.** This study is based on the ERA-Interim dataset available on-
432 line at <https://apps.ecmwf.int/datasets/data/interim-full-moda/levtype=pl/>,
433 the NOAA interpolated OLR dataset available online at [https://psl.noaa.gov/](https://psl.noaa.gov/data/gridded/data.interp_OLR.html)
434 [data/gridded/data.interp_OLR.html](https://psl.noaa.gov/data/gridded/data.interp_OLR.html), and the GPCP dataset available online at
435 <https://psl.noaa.gov/data/gridded/data.gpcp.html>. The OISST data is avail-
436 able online at [https://www.esrl.noaa.gov/psd/data/gridded/data.noaa.oisst.v2.](https://www.esrl.noaa.gov/psd/data/gridded/data.noaa.oisst.v2.highres.html)
437 [highres.html](https://www.esrl.noaa.gov/psd/data/gridded/data.noaa.oisst.v2.highres.html). The first author is supported by the Japan Society for the Promotion
438 of Science (JSPS)-Kakenhi Grant Number 19K23460 and 20K14554. The third author is
439 supported by JSPS-Kakenhi Grant Number 16H04048. The fourth author is supported

440 by JSPS-Kakenhi Grant Number 20J00605. The numerical computations using NICAM
441 is performed on a super computer, Oakforest-PACS.

References

- 442 Adler, R. F., G. J. Huffman, A. Chang, R. Ferraro, P.-P. Xie, J. Janowiak, B. Rudolf,
443 U. Schneider, S. Curtis, D. Bolvin, et al. (2003), The version-2 global precipitation
444 climatology project (gpcp) monthly precipitation analysis (1979–present), *J. Hydrome-*
445 *teor.*, *4*(6), 1147–1167.
- 446 Bjerknes, J. (1969), Atmospheric teleconnections from the equatorial Pacific, *Mon. Wea.*
447 *Rev.*, *97*(3), 163–172.
- 448 Camberlin, P. (1995), June-september rainfall in north-eastern Africa and atmospheric
449 signals over the tropics: A zonal perspective, *International Journal of Climatology*,
450 *15*(7), 773–783.
- 451 Camberlin, P., and N. Philippon (2002), The East African March–May rainy season: As-
452 sociated atmospheric dynamics and predictability over the 1968–97 period, *J. Climate*,
453 *15*(9), 1002–1019.
- 454 Chakraborty, A., R. S. Nanjundiah, and J. Srinivasan (2009), Impact of African orography
455 and the Indian summer monsoon on the low-level Somali jet, *Int. J. Climatol.*, *29*(7),
456 983–992.
- 457 Chou, C., and J. D. Neelin (2003), Mechanisms limiting the northward extent of the
458 northern summer monsoons over North America, Asia, and Africa, *J. Climate*, *16*(3),
459 406–425.

- 460 Dee, D. P., S. M. Uppala, A. Simmons, P. Berrisford, P. Poli, S. Kobayashi, U. Andrae,
461 M. Balmaseda, G. Balsamo, d. P. Bauer, et al. (2011), The ERA-Interim reanalysis:
462 Configuration and performance of the data assimilation system, *Quart. J. Roy. Meteor.
463 Soc.*, *137*(656), 553–597.
- 464 Findlater, J. (1969), A major low-level air current near the Indian Ocean during the
465 northern summer, *Quarterly Journal of the Royal Meteorological Society*, *95*(404), 362–
466 380.
- 467 Hartman, A. T. (2018), An analysis of the effects of temperatures and circulations on
468 the strength of the low-level jet in the Turkana Channel in East Africa, *Theor. Appl.
469 Climatol.*, *132*(3), 1003–1017.
- 470 Hastenrath, S., D. Polzin, and L. Greischar (2002), Annual cycle of equatorial zonal
471 circulations from the ECMWF reanalysis, *J. Meteor. Soc. Japan*, *80*(4), 755–766.
- 472 Heaviside, C., and A. Czaja (2013), Deconstructing the Hadley cell heat transport, *Quart.
473 J. Roy. Meteor. Soc.*, *139*(677), 2181–2189.
- 474 King, J. A., R. Washington, and S. Engelstaedter (2021), Representation of the Indian
475 Ocean Walker circulation in climate models and links to kenyan rainfall, *Int. J. Clima-
476 tol.*, *41*, E616–E643.
- 477 Kodama, C., Y. Yamada, A. T. Noda, K. Kikuchi, Y. Kajikawa, T. Nasuno, T. Tomita,
478 T. Yamaura, H. G. Takahashi, M. Hara, et al. (2015), A 20-year climatology of a NICAM
479 AMIP-type simulation, *Journal of the Meteorological Society of Japan. Ser. II*, *93*(4),
480 393–424.
- 481 Kodama, C., T. Ohno, T. Seiki, H. Yashiro, A. T. Noda, M. Nakano, Y. Yamada,
482 W. Roh, M. Satoh, T. Nitta, D. Goto, H. Miura, T. Nasuno, T. Miyakawa, Y.-W.

- 483 Chen, and M. Sugi (2020), The non-hydrostatic global atmospheric model for cmip6
484 highresmip simulations (nicam16-s): Experimental design, model description, and sen-
485 sitivity experiments, *Geoscientific Model Development Discussions*, 2020, 1–50, doi:
486 10.5194/gmd-2019-369.
- 487 Lau, K., and S. Yang (2003), Walker circulation, *Encyclopedia of atmospheric sciences*,
488 pp. 2505–2510.
- 489 Liebmann, B., and C. A. Smith (1996), Description of a complete (interpolated) outgoing
490 longwave radiation dataset, *Bull. Amer. Meteor. Soc.*, 77(6), 1275–1277.
- 491 Liebmann, B., M. P. Hoerling, C. Funk, I. Bladé, R. M. Dole, D. Allured, X. Quan,
492 P. Pegion, and J. K. Eischeid (2014), Understanding recent eastern Horn of Africa
493 rainfall variability and change, *Journal of Climate*, 27(23), 8630–8645.
- 494 Liebmann, B., I. Bladé, C. Funk, D. Allured, X.-W. Quan, M. Hoerling, A. Hoell, P. Peter-
495 son, and W. M. Thiaw (2017), Climatology and interannual variability of boreal spring
496 wet season precipitation in the eastern horn of africa and implications for its recent
497 decline, *Journal of Climate*, 30(10), 3867–3886.
- 498 Louis, J.-F. (1979), A parametric model of vertical eddy fluxes in the atmosphere,
499 *Boundary-Layer Meteorology*, 17(2), 187–202.
- 500 Lyon, B. (2014), Seasonal drought in the Greater Horn of Africa and its recent increase
501 during the March–May long rains, *Journal of Climate*, 27(21), 7953–7975.
- 502 Mellor, G. L., and T. Yamada (1982), Development of a turbulence closure model for
503 geophysical fluid problems, *Reviews of Geophysics*, 20(4), 851–875.
- 504 Munday, C., R. Washington, and N. Hart (2021), African low-level jets and their
505 importance for water vapor transport and rainfall, *Geophys. Res. Lett.*, 48(1),

506 e2020GL090,999.

507 Naiman, Z., P. J. Goodman, J. P. Krasting, S. L. Malyshev, J. L. Russell, R. J. Stouffer,
508 and A. T. Wittenberg (2017), Impact of mountains on tropical circulation in two Earth
509 system models, *Journal of Climate*, *30*(11), 4149–4163.

510 Nakanishi, M., and H. Niino (2004), An improved Mellor–Yamada level-3 model with
511 condensation physics: Its design and verification, *Boundary-layer meteorology*, *112*(1),
512 1–31.

513 NCEP (2015), NCEP GDAS/FNL 0.25 degree global tropospheric analyses and forecast
514 grids.

515 Nicholson, S. (2016), The Turkana low-level jet: mean climatology and association with
516 regional aridity, *Int. J. Climatol.*, *36*(6), 2598–2614.

517 Nicholson, S. E. (2018), The ITCZ and the seasonal cycle over equatorial africa, *Bull.*
518 *Amer. Meteor. Soc.*, *99*(2), 337–348.

519 Noda, A. T., K. Oouchi, M. Satoh, H. Tomita, S.-i. Iga, and Y. Tsushima (2010), Im-
520 portance of the subgrid-scale turbulent moist process: Cloud distribution in global
521 cloud-resolving simulations, *Atmospheric Research*, *96*(2-3), 208–217.

522 Ogallo, L. (1988), Relationships between seasonal rainfall in East Africa and the Southern
523 Oscillation, *J. Climatol.*, *8*(1), 31–43.

524 Ogwang, B. A., H. Chen, X. Li, and C. Gao (2014), The influence of topography on East
525 African October to December climate: sensitivity experiments with RegCM4, *Adv.*
526 *Meteor.*, *2014*.

527 Reynolds, R. W., T. M. Smith, C. Liu, D. B. Chelton, K. S. Casey, and M. G. Schlax
528 (2007), Daily high-resolution-blended analyses for sea surface temperature, *J. Climate*,

- 529 20(22), 5473–5496.
- 530 Rodwell, M. J., and B. J. Hoskins (1995), A model of the Asian summer monsoon. Part
531 II: Cross-equatorial flow and PV behavior, *J. Atmos. Sci.*, 52(9), 1341–1356.
- 532 Saji, N., B. Goswami, P. Vinayachandran, and T. Yamagata (1999), A dipole mode in the
533 tropical indian ocean, *Nature*, 401(6751), 360–363.
- 534 Satoh, M., T. Matsuno, H. Tomita, H. Miura, T. Nasuno, and S.-i. Iga (2008), Nonhydro-
535 static icosahedral atmospheric model (NICAM) for global cloud resolving simulations,
536 *Journal of Computational Physics*, 227(7), 3486–3514.
- 537 Satoh, M., H. Tomita, H. Yashiro, H. Miura, C. Kodama, T. Seiki, A. T. Noda, Y. Yamada,
538 D. Goto, M. Sawada, et al. (2014), The non-hydrostatic icosahedral atmospheric model:
539 Description and development, *Progress in Earth and Planetary Science*, 1(1), 18.
- 540 Schreck III, C. J., and F. H. Semazzi (2004), Variability of the recent climate of eastern
541 Africa, *International Journal of Climatology: A Journal of the Royal Meteorological*
542 *Society*, 24(6), 681–701.
- 543 Schwendike, J., P. Govekar, M. J. Reeder, R. Wardle, G. J. Berry, and C. Jakob (2014),
544 Local partitioning of the overturning circulation in the tropics and the connection to
545 the Hadley and Walker circulations, *J. Geophys. Res.*, 119(3), 1322–1339.
- 546 Sekiguchi, M., and T. Nakajima (2008), A k-distribution-based radiation code and its
547 computational optimization for an atmospheric general circulation model, *Journal of*
548 *Quantitative Spectroscopy and Radiative Transfer*, 109(17-18), 2779–2793.
- 549 Slingo, J., H. Spencer, B. Hoskins, P. Berrisford, and E. Black (2005), The meteorology
550 of the Western Indian Ocean, and the influence of the East African Highlands, *Philos.*
551 *Trans. R. Soc. A*, 363(1826), 25–42.

- 552 Sobel, A. H., J. Nilsson, and L. M. Polvani (2001), The weak temperature gradient ap-
553 proximation and balanced tropical moisture waves, *J. Atmos. Sci.*, *58*(23), 3650–3665.
- 554 Takata, K., S. Emori, and T. Watanabe (2003), Development of the minimal advanced
555 treatments of surface interaction and runoff, *Global and planetary Change*, *38*(1-2),
556 209–222.
- 557 Tanaka, H. L., N. Ishizaki, and A. Kitoh (2004), Trend and interannual variability of
558 Walker, monsoon and Hadley circulations defined by velocity potential in the upper
559 troposphere, *Tellus A*, *56*(3), 250–269.
- 560 Tierney, J. E., C. C. Ummenhofer, and P. B. deMenocal (2015), Past and future rainfall
561 in the Horn of Africa, *Sci. Adv.*, *1*(9), e1500,682.
- 562 Tomita, H. (2008), New microphysical schemes with five and six categories by diagnostic
563 generation of cloud ice, *Journal of the Meteorological Society of Japan. Ser. II*, *86*,
564 121–142.
- 565 Tomita, H., and M. Satoh (2004), A new dynamical framework of nonhydrostatic global
566 model using the icosahedral grid, *Fluid Dynamics Research*, *34*(6), 357.
- 567 Tomita, H., M. Satoh, and K. Goto (2002), An optimization of the icosahedral grid
568 modified by spring dynamics, *J. Comput. Phys.*, *183*(1), 307–331.
- 569 Uno, I., X.-M. Cai, D. Steyn, and S. Emori (1995), A simple extension of the Louis method
570 for rough surface layer modelling, *Boundary-layer meteorology*, *76*(4), 395–409.
- 571 Veiga, J. A. P., V. B. Rao, and S. H. Franchito (2011), Annual mean analysis of the
572 tropical heat balance and associations with the Walker circulation, *Revista Brasileira
573 de Meteorologia*, *26*(1), 01–08.

- 574 Vizzy, E. K., and K. H. Cook (2019), Observed relationship between the Turkana low-level
575 jet and boreal summer convection, *Climate Dyn.*, *53*(7), 4037–4058.
- 576 Walker, G. T. (1923), Correlations in seasonal variation of weather, VIII: A preliminary
577 study of world weather, *Mem. Indian Meteorol. Dep.*, *24*, 75–131.
- 578 Walker, G. T. (1924), Correlations in seasonal variations of weather, IX: A further study
579 of world weather, *Mem. Indian Meteorol. Dep.*, *24*, 275–332.
- 580 Williams, A. P., and C. Funk (2011), A westward extension of the warm pool leads to
581 a westward extension of the Walker circulation, drying eastern africa, *Climate Dyn.*,
582 *37*(11-12), 2417–2435.
- 583 Yang, W., R. Seager, M. A. Cane, and B. Lyon (2014), The East African long rains in
584 observations and models, *J. Climate*, *27*(19), 7185–7202.
- 585 Yang, W., R. Seager, M. A. Cane, and B. Lyon (2015), The annual cycle of East African
586 precipitation, *J. Climate*, *28*(6), 2385–2404.
- 587 Zhao, S., and K. H. Cook (2021), Influence of Walker circulations on East African rainfall,
588 *Climate Dyn.*, pp. 1–21.

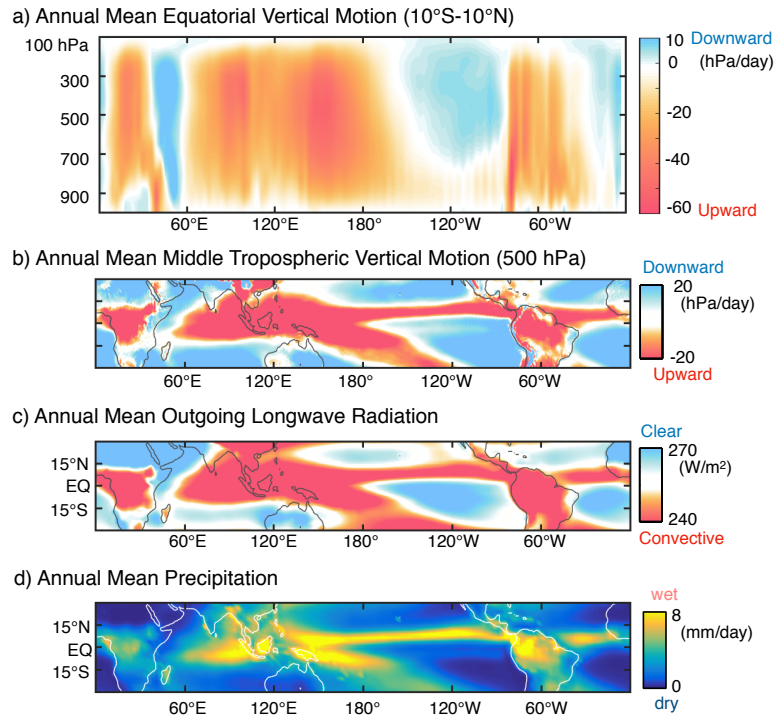


Figure 1. (a): Observed annual-mean vertical motion averaged meridionally over the equatorial region (10°S-10°N) based on the ERA-Interim Reanalysis data. (b): As in (a), but the horizontal map at 500 hPa. (c): Observed annual-mean outgoing longwave radiation (OLR) based on the NOAA interpolated OLR data. (d): Observed annual-mean precipitation based on the GPCP data.

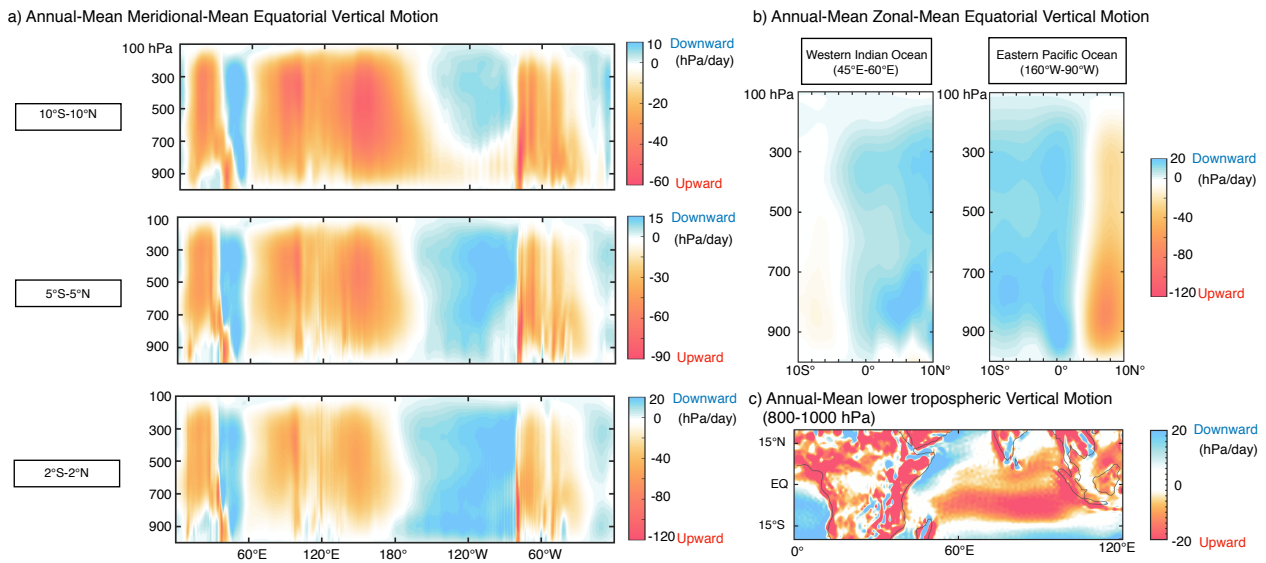


Figure 2. (a): As in Fig. 1a, but over the equatorial belt of 10°S-10°N (top) , 5°S-5°N (middle), and 2°S-2°N (bottom). (b): Observed annual-mean vertical motion averaged zonally over the Western Indian Ocean (45°E-60°E) and the Eastern Pacific Ocean (160°W-90°W). (c): Observed annual-mean vertical motion averaged vertically over the lower troposphere (800-1000hPa). All panels are produced based on the ERA-Interim Reanalysis data.

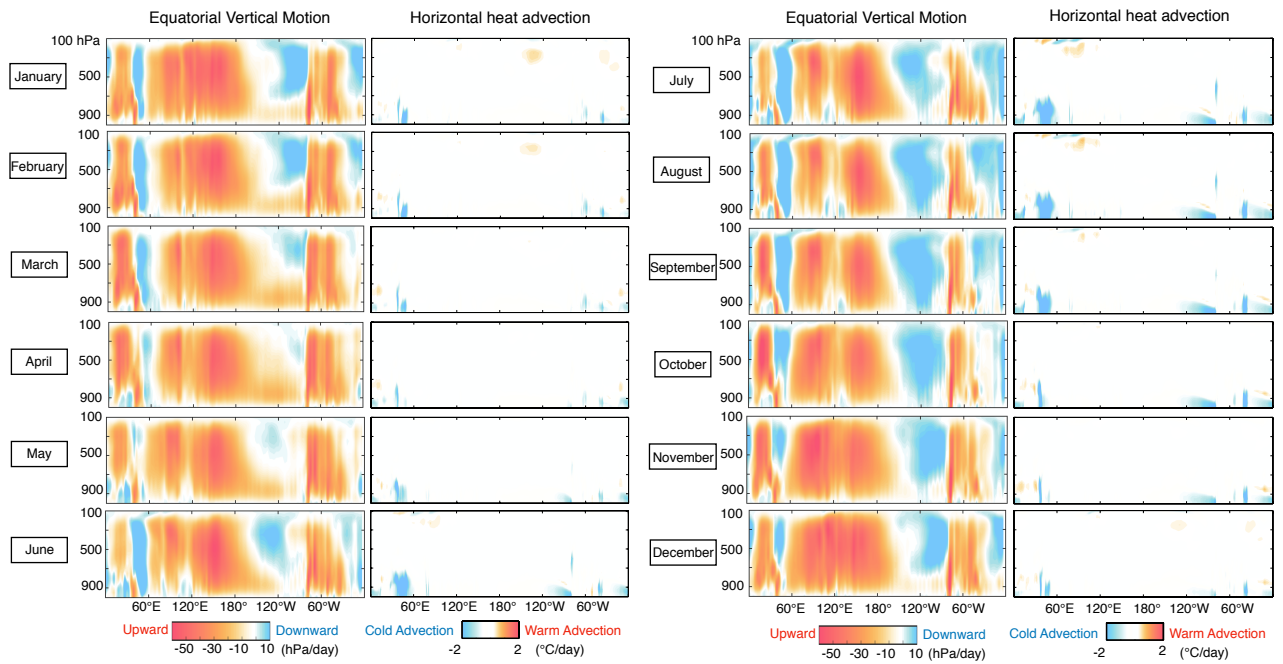


Figure 3. Left columns, As in Fig. 1a, but monthly mean values for each month averaged over 1979-2017. Right columns, As in right, but for mean horizontal advection defined as the inner product of mean horizontal wind and the horizontal gradient of mean temperature. All panels are produced based on the ERA-Interim Reanalysis data.

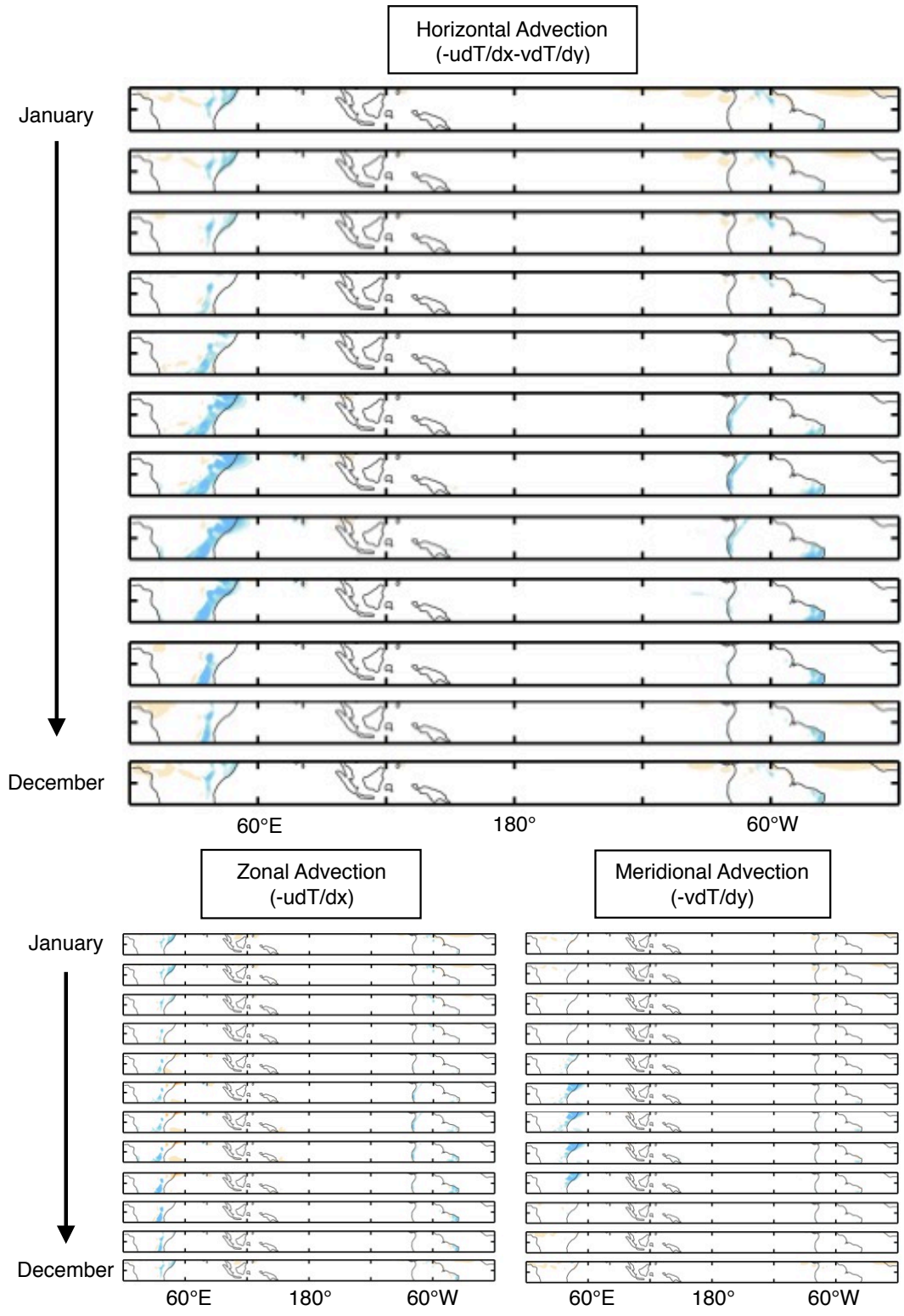


Figure 4. As in the right columns of Fig. 3, but for vertical-mean tropospheric horizontal advection (top), zonal advection (bottom left), and meridional advection (bottom right) taken for the 100-1000 hPa layer. Contribution of eddy transport is not considered. All panels are produced based on the ERA-Interim Reanalysis data.

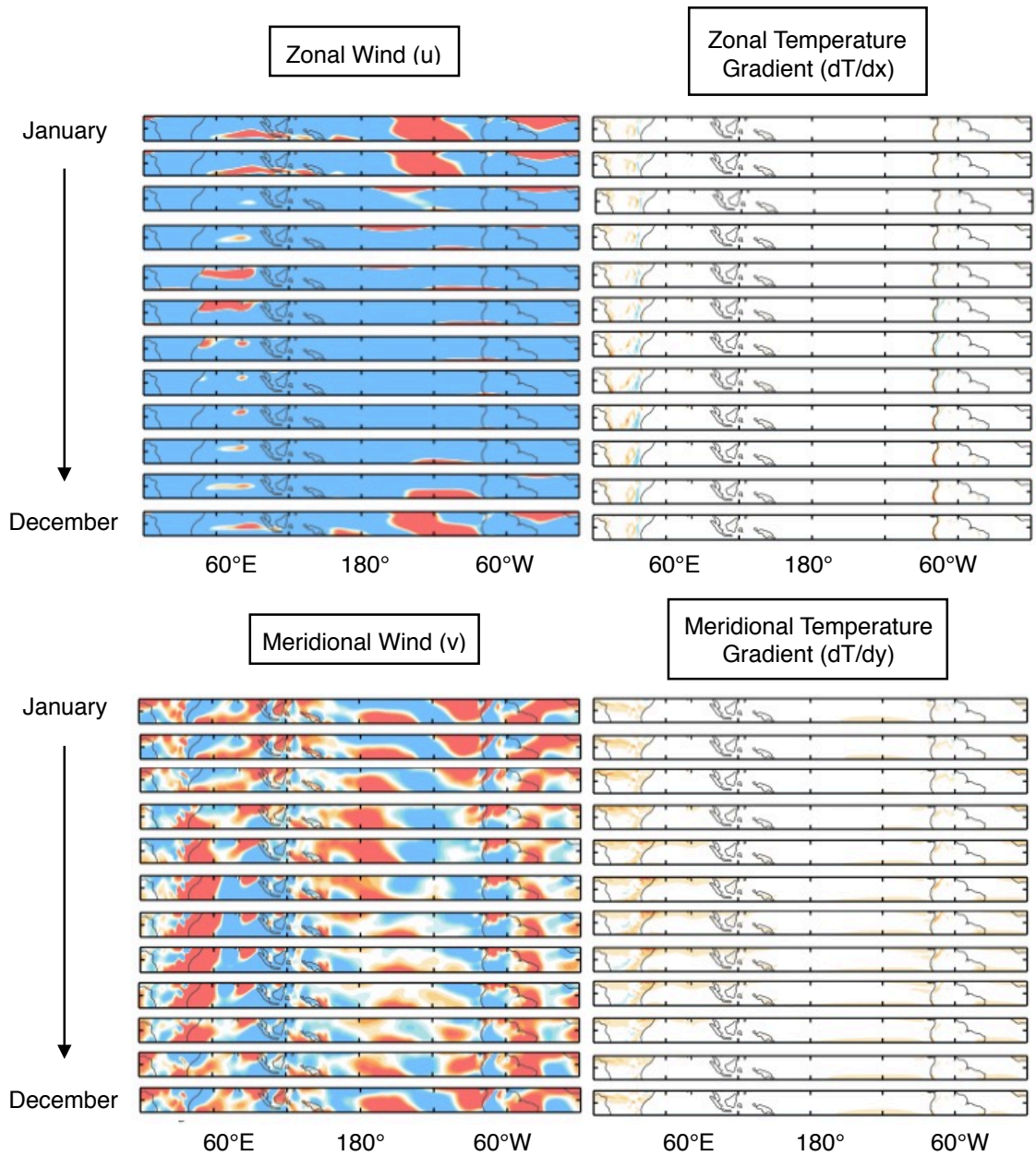


Figure 5. As in Fig. 4, but for zonal wind (top left), zonal temperature gradient (top right), meridional wind (bottom left), and meridional temperature gradient (bottom right). All panels are produced based on the ERA-Interim Reanalysis data.

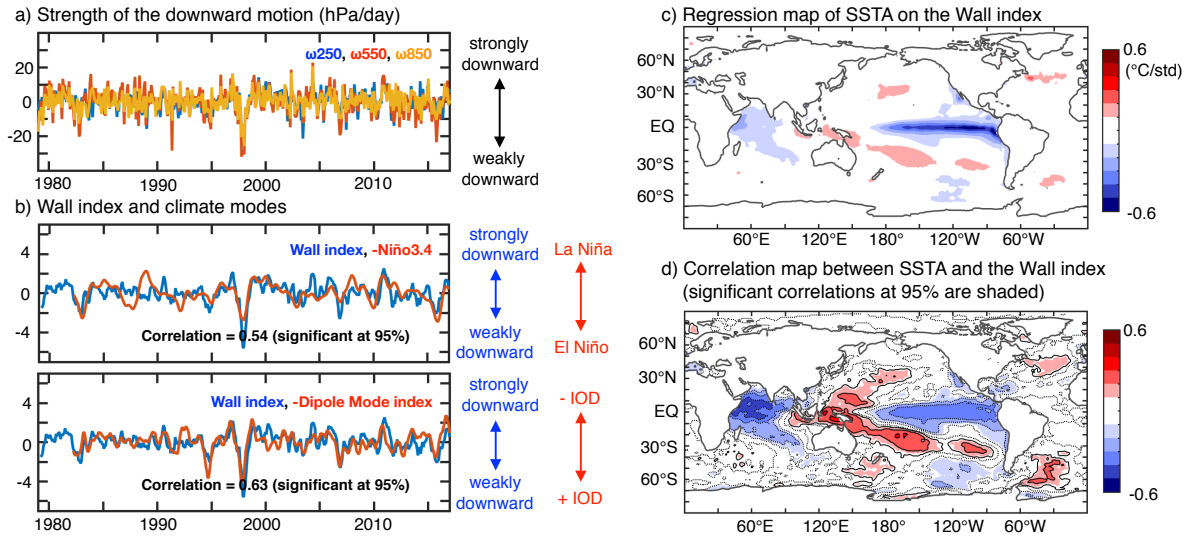


Figure 6. (a): Time series of the observed monthly-mean vertical motion at 250 hPa (blue), 550 hPa (red), and 850 hPa (yellow), averaged over the Wall region (10°S-10°N, 40°E-60°E). (b): Top, Monthly-mean time series of the Wall index defined as the mean of the three time series shown in (a) standardized by its own standard deviation (blue). Also shown is the monthly-mean Niño 3.4 index defined as the regional-mean sea surface temperature anomalies (SSTA) over the Niño 3.4 region (5°S-5°N, 170°W-120°W) standardized by its own standard deviation and the sign is reversed (red). Bottom, As in top, but for the Dipole Mode Index defined as the SSTA difference calculated in the manner of the western equatorial Indian Ocean (50°E-70°E and 10°S-10°N) minus the south eastern equatorial Indian Ocean (90°E-110°E and 10°S-0°N). (c): Regression map of SSTA on the monthly-mean Wall index. (d) Correlation map between SSTA and the monthly-mean Wall index. Contour interval is 0.1, and only statistically significant correlations at the 95% confidence level are shaded.

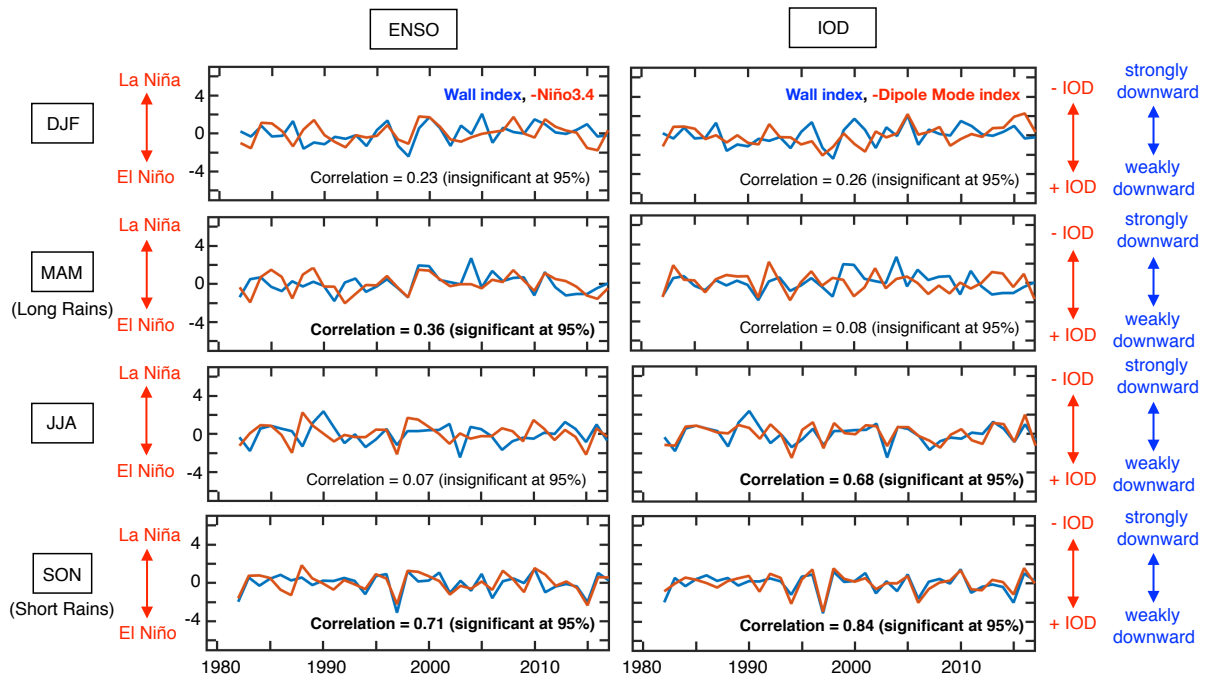


Figure 7. Left, As in the top panel in Fig. 6b, but for seasonal-mean time series for December-January-February (DJF), March-April-May (MAM), June-July-August (JJA), and September-October-November (SON). Right, As in left, but for the bottom panel in Fig. 6b.

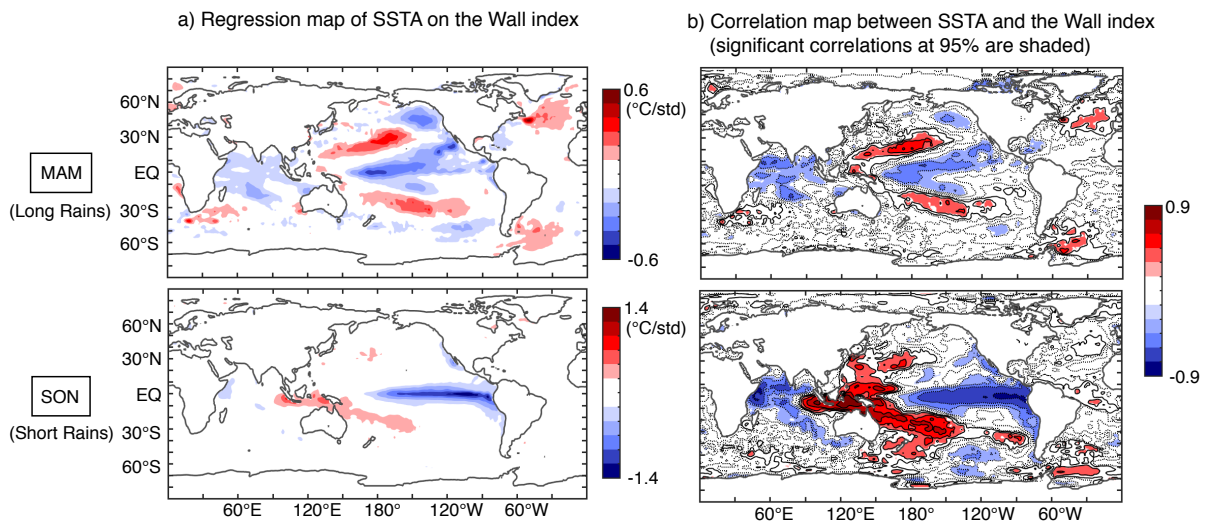


Figure 8. (a): As in Fig. 6c, but for seasonal-mean time series for March-April-May (MAM) and September-October-November (SON). (b): As in Fig. 6d, but for seasonal-mean time series for March-April-May (MAM) and September-October-November (SON). Contour interval is 0.15.

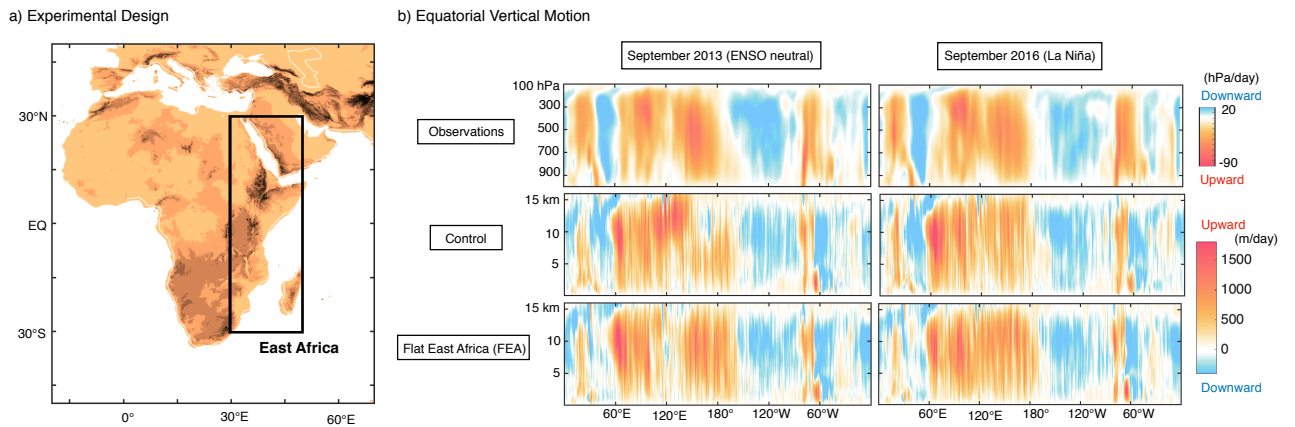


Figure 9. (a): Topography of the entire African continent based on the Global 30-Arc-Second DEM project (GTOPO30) data, which is used as the lower boundary condition for the model runs. Black box shows the East African region (30°S-30°N, 30°E-50°E). (b): As in Fig. 1a, but for one-month mean values calculated for September 2013 (left) and 2016 (right) based on observations, the control, and the Flat East Africa (FEA) experiment in this order from the top panel. In the FEA experiment, the topography in the East African region, shown as the black box in (a), is flattened and set to be 1 meter.

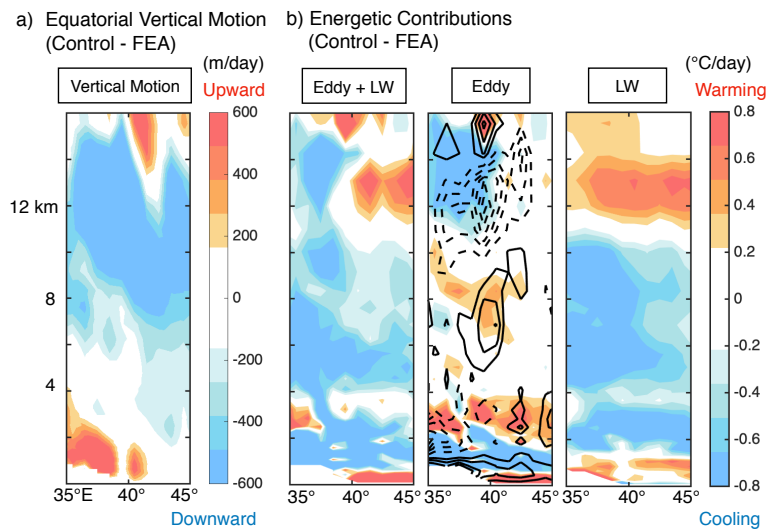


Figure 10. (a): The difference of one-month mean vertical motion for September 2016 between the control and FEA runs in 35°E-45°E. (b): As in (a), but the energetic tendency contributions by the sum of eddy heat transport and longwave radiation (left), eddy heat transport (middle), and longwave radiation (right). Also shown as contours in the middle panel is eddy vertical momentum transport. Solid (dashed) curves denote upward (downward) vertical momentum transport. Contour interval is 0.05 (m/s)/day.

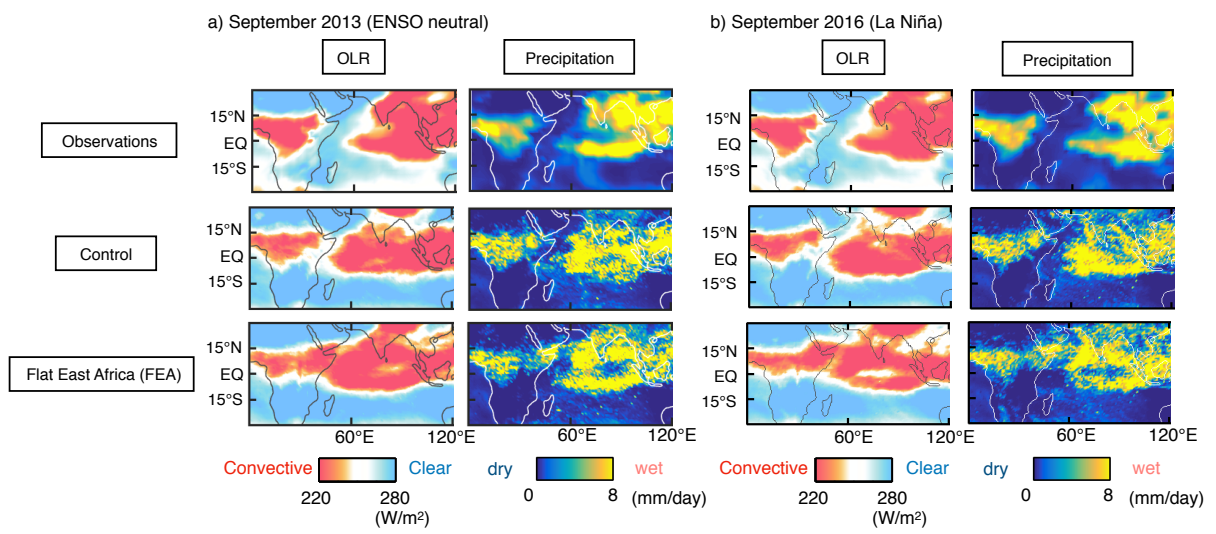


Figure 11. (a): As in Fig. 9b, but for OLR (left) and precipitation (right) for 2013. (b): As in (a), but for 2016.